

Practical insights on the effect of different encodings, ansätze and measurements in quantum and hybrid convolutional neural networks

Jesús Lozano-Cruz ^{†,1,*} Albert Nieto-Morales ^{†,1,2,*} Oriol Balló-Gimbernat ^{3,4,5,*}
Adan Garriga ^{3,*} Antón Rodríguez-Otero^{6,*} and Alejandro Borrallo-Rentero^{6,*}

¹*Quantum Lab, CTIC Centro Tecnológico, Parque Científico Tecnológico de Gijón, Asturias, Spain*

²*Universidad Internacional de la Rioja (UNIR), Logroño, Spain*

³*Eurecat, Centre Tecnològic de Catalunya, Multimedia Technologies, Barcelona, Spain*

⁴*Centre de Visió per Computador (CVC), Barcelona, Spain.*

⁵*Universitat Autònoma de Barcelona (UAB), Barcelona, Spain.*

⁶*Fsas International Quantum Center (Fujitsu), Santiago de Compostela, Spain.*

(Dated: June 26, 2025)

This study investigates the design choices of parameterized quantum circuits (PQCs) within quantum and hybrid convolutional neural network (HQNN and QCNN) architectures, applied to the task of satellite image classification using the EuroSAT dataset. We systematically evaluate the performance implications of data encoding techniques, variational ansätze, and measurement in ≈ 500 distinct model configurations. Our analysis reveals a clear hierarchy of influence on model performance. For hybrid architectures, which were benchmarked against their direct classical equivalents (e.g. the same architecture with the PQCs removed), the data encoding strategy is the dominant factor, with validation accuracy varying over 30% for distinct embeddings. In contrast, the selection of variational ansätze and measurement basis had a comparatively marginal effect, with validation accuracy variations remaining below 5%. For purely quantum models, restricted to amplitude encoding, performance was most dependent on the measurement protocol and the data-to-amplitude mapping. The measurement strategy varied the validation accuracy by up to 30% and the encoding mapping by around 8 percentage points.

Keywords: quantum machine learning, parameterized quantum circuit, image classification, quantum neural network, ansatz

In recent years, quantum machine learning (QML) has emerged as an interdisciplinary field at the intersection of quantum computing and machine learning [1–4]. Its objective is to leverage phenomena in quantum mechanics to tackle problems from machine learning. A central component of many contemporary QML models is the parameterized quantum circuit (PQC), a flexible framework for creating trainable quantum circuits that can be used independently or integrated as hybrid components within classical neural networks (NNs).

This work investigates the use PQCs for the task of satellite image classification using the EuroSAT dataset [5]. These PQCs serve as trainable quantum components that can be integrated into NNs or used by themselves. While PQCs offer a flexible paradigm for hybrid and purely QML models, their efficacy is highly sensitive to a multitude of design choices, with the most important being: the encoding technique, the ansätze and the measurement strategy.

We study two different hybrid architectures networks and a purely quantum one, all inspired by convolutional neural networks (CNN). For the hybrid ones we have a “quantum first” model, in which PQCs are used as convolutions to extract features, and a “quantum later” model [6], in which PQCs are used between the fully

connected layers to process the extracted features [6–8]. For the quantum architecture, we use three variations of PQCs as standalone components, one of which inspired by the QCNN, introduced in [9].

Our approach builds on the work of [10], which systematically benchmarked different quantum machine learning models by varying the encoding, measurement and hyperparameters. Our difference lies in the fact that we fix the hyperparameters and benchmark our hybrid and purely quantum models across all three key circuit components: encoding, ansätze and measurement.

The primary objective of this work is not necessarily to achieve state-of-the-art performance, or claim quantum utility, but rather to find practical insights into how core PQC design elements influence model behavior and efficacy. The findings are intended to aid researchers and practitioners in designing QML models.

All our experiments were done through simulations using the *CTIC Quantum Testbed (QUTE)* platform [11]. We used PennyLane [12] to implement the PQCs, both in the purely quantum and hybrid models, and PyTorch [13] for the classical layers.

A. Image classification

Our focus will be in classifying satellite images from the EuroSAT dataset [5], examples can be seen in FIG. 1. The dataset consists of 27,000 geo-referenced images, provided by the Copernicus Earth observation pro-

[†] Corresponding authors: jesus.lozano@fundacionctic.org and albert.nieto@unir.net

* All authors contributed equally to this work.

gram [14] using the Sentinel-2 satellite, and comes in two versions: RGB and all bands. The first consists of only RGB channels and the other uses all the bands of the spectrum as collected from Sentinel-2. Each image channel has a resolution of 64×64 pixels.

In our experiments, we used the RGB version and downsampled them to 32×32 and 16×16 . The former was only studied for the hybrid models, due computation constraints, and the latter for both hybrid and purely quantum models.

We selected this dataset as a continuation of the work conducted within the ARQA Cervera Technology Transfer Network [15]. Nevertheless, identical experiments can be replicated on alternative datasets, provided they satisfy the previously established size constraints.



FIG. 1: Samples from the EuroSAT dataset introduced in [5]. Each sample is a $64 \times 64 \times 3$ RGB image obtained from the Sentinel-2 satellite.

B. Parameterized quantum circuits

PQCs are the cornerstone of our approach. We integrate them as layers consisting of one or more circuits in the hybrid models and use them by themselves in the purely quantum ones. In general, PQCs consist of three key components: encoding, used to embed the information in a quantum state, variational ansatz, used to manipulate the encoded information, and measurement, used to extract information from the quantum state. FIG. 2 shows the prototypical example of a PQC.

1. Data encoding

As previously mentioned, the first stage in a PQC is the data encoding, this step serves as a mapping from data to a quantum state. Given that there is not a one size fits all solution for the encoding step, we chose to include the following ones into our analysis:

- **Angle encoding** [4, 16, 17]: This is a prevalent and relatively straightforward method where N classical data features, x_1, x_2, \dots, x_N , are encoded into the rotation angles of N individual qubits. Each feature x_j is used as an angle parameter

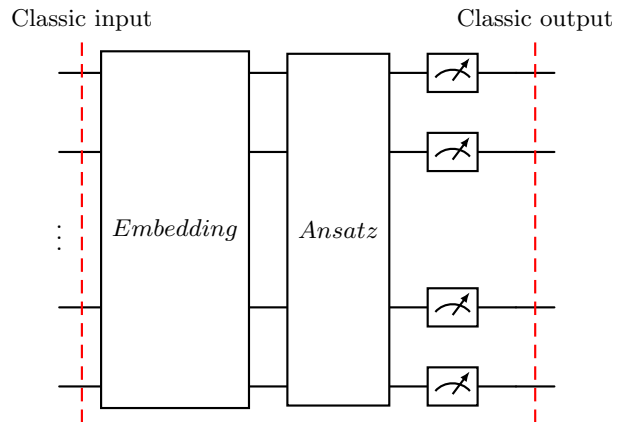


FIG. 2: Prototypical quantum circuit scheme.

for a single-qubit rotation gate, such as $R_X(\theta_j)$, $R_Y(\theta_j)$, or $R_Z(\theta_j)$, applied to a specific qubit. Notably, using $R_Z(\theta_j)$ as an encoding gate acting on an initial initial state from the computational basis only adds an irrelevant global phase.

- **Amplitude encoding** [4]: This technique embeds a classical data vector of 2^n normalized real numbers, $\{\alpha_i\}$, directly into the amplitudes of an n -qubit quantum state vector $|\Psi\rangle$. The state is represented as:

$$|\Psi\rangle = \sum_{i=0}^{2^n-1} \alpha_i |i\rangle$$

where $|i\rangle$ are the computational basis states, and the amplitudes must satisfy the normalization condition $\sum_{i=0}^{2^n-1} |\alpha_i|^2 = 1$. The state preparation process required to achieve an arbitrary state $|\Psi\rangle$ can be computationally expensive, potentially demanding an exponentially deep circuit [18].

- **Instantaneous quantum polynomial-time (IQP) encoding** [19]: This encoding extends the concept of angle encoding by incorporating entangling operations. N classical features are typically encoded into N qubits using single-qubit rotations, akin to angle encoding. These rotations are then interspersed with diagonal two-qubit gates, commonly $R_{ZZ}(\phi_{jk})$ gates, where ϕ_{jk} can be a function of individual features or products of features (e.g., $x_j x_k$). This structure allows for the generation of more complex quantum states that can potentially capture correlations between input features. The number of layers is a tunable parameter.
- **Quantum approximate optimization algorithm (QAOA) inspired encoding** [20]: This encoding strategy draws inspiration from the structure of the QAOA. It transforms N classical features into parameters that define a QAOA-like

ansatz applied to N qubits. The features typically determine the angles for rotation gates within layers corresponding to a problem Hamiltonian and a mixer Hamiltonian. The number of layers is a tunable parameter and there are 3 variants: X , Y and Z .

- **Ring encoding** [21]: This method combines angle encoding for N features on N qubits with a specific entangling topology. Following initial single-qubit rotations that embed the classical data, two-qubit entangling gates are applied between adjacent qubits arranged in a ring structure. Specifically, qubit i is entangled with qubit $(i+1) \bmod N$. The number of layers is a tunable parameter.
- **Waterfall encoding** [21]: Similar to Ring Encoding, Waterfall Encoding also utilizes angle encoding for N features on N qubits, followed by a structured application of entangling gates. In this scheme, the entangling gates are typically arranged in a “waterfall” pattern. For example, qubit i might control an operation on qubit $i+1$, which in turn might control an operation on qubit $i+2$, and so forth.

2. Variational ansatz

The variational circuit constitutes the second part of a PQC. It consists of a set of quantum gates with trainable parameters, akin to neurons in a NN. Its purpose is to manipulate the quantum state generated by the previous step with the goal of turning it into a state whose measurement, in a given basis, solves the task in hand. We chose to experiment with the following ones:

- **No entangled**: This circuit uses randomness in the assignment of quantum gates, applying either an RZ gate or the identity operation to each qubit in a stochastic manner. Due to the potential presence of trivial operations (identity), the resulting circuit typically exhibits a lower computational depth compared to more densely parameterized or entangled circuits.
- **Fully entangled** [22]: This circuit is implemented using the `StronglyEntanglingLayers` module from PennyLane [12]. It allows for a configurable number of layers, each consisting of a sequence of single-qubit rotations followed by entangling operations. This structure enables flexible depth and entanglement patterns suitable for a variety of variational quantum algorithms.
- **Ring circuit** [21]: It performs single-qubit rotations using RY and RZ gates, followed by the application of controlled- Z (CZ) gates arranged in a ring topology. The resulting structure resembles

the ring embedding, but with entanglement introduced through CZ operations instead of $CNOT$.

- **NQ circuit** [23]: The circuit consists of multiple layers, each combining parameterized single-qubit rotations, RY and RZ , followed by entangling gates ($CNOT$) in a linear nearest-neighbor topology.
- **QCNN circuit** [9]: circuit structure inspired by classical CNNs in which convolutional and pooling operations are subsequently applied in each layer. In our implementation, when the number of qubits at a layer is odd, one is excluded from the pooling, although it is still considered in the convolutional stages. At the end of the circuit, the qubits that were discarded are recovered for the fully connected layer. Given that the number of free parameters in an arbitrary unitary scales as $4^N - 1$, we substituted this last operation by the *Simplified Two Design* [24].

3. Measurement

The final step of a PQC is the measurement; at this stage, either all or only a fraction of the qubits are measured to extract classical information. This information can then be used to update parameters, feed the next layer in a hybrid network, or serve as the final output. In pure quantum models, we do not need to measure until the end of the network. We tested with 3 measurements in the hybrid case.

- **Z-basis**: It is also called the computational basis, this is the most commonly used measurement in quantum circuits because it collapses a qubit into $|0\rangle$ or $|1\rangle$.
- **X-basis**: In this case, a Hadamard gate (H) is applied before measuring in the Z-basis. It is often used in entangled states.
- **Y-basis**: Now, the inverse of a phase gate (S^\dagger) is applied and then measures in the X-basis. This is typically employed in phase-sensitive protocols.

In the fully quantum models, in order to have more flexibility when it comes to the amount of classical information we can extract out of a circuit, we also measured multiqubit observables:

- **Histogram**: We measure each qubit on the Z basis and count the frequency of each of the possible 2^N outcomes, for N qubits. Each state is associated with a class, hence the model in this case will try to learn to link classes with corresponding states. This is in essence a Quantum Circuit Born Machine [25] in which we set the most frequent sample to be the predicted class label.

- **Pauli string (Paulis):** We estimate the expectation value of pauli strings of N qubits, i.e., observables of the form: $O = \otimes_{i=0}^N P_i$, where P_i is a Pauli gate acting on the i -th qubit. Here, a class is identified with an operator such that the model is trained to maximize the expectation value of that observable when images from the correct class are fed into the model.

Recent studies have also pointed out the relevance of the type of measurement considered in the models [26].

I. MODELS

For an overview of the models see TABLE I.

A. Hybrid models I: HQNN-Parallel

The *HQNN-Parallel* was firstly introduced in [6] (shown in FIG. 4a). This architecture introduces NN layer based on multiple PQCs. From this point onward, we will call this a quantum linear layer due to its similarity with a classical linear layer.

A quantum linear layer operates in a similar manner as its classical counterpart. It takes in an input vector of size V and outputs another of size W . However, unlike the classical case, here $W \leq V$ given that at most we do a single measurement on all qubits. In the classical version, the linear layer is defined by the number of input and output features. The quantum analog is characterized by the number of input features, the number of qubits allocated per circuit, same number for all, and the encoding used, which will determine the proportion between input and output features.

In the simplest case, we have an input vector of length L , we allocate $L/2$ qubits per circuit and use an encoding that maps a single feature to a single qubit, like angle encoding. In this case, the quantum linear layer will consist of two PQCs of $L/2$ qubits each, and the output will be a vector of length L , given that we measure all qubits on a given basis. This scheme is shown in FIG. 3. For instance, if we use amplitude embedding, then each N qubit circuit will process 2^N features and the output will be of size $N \times$ the number of circuits.

This architecture scales really well with the available quantum resources, given that you can tune the number of qubits allocated per circuit. The higher the per circuit qubit count, more correlations between features will be accessible and better performance is expected. Also, given that all circuits are independent, they can be executed in parallel.

In all our experiments for this architecture the feature vectors were of size 768 and we allocated 8 qubits per circuit. Both for the $32 \times 32 \times 3$ and $16 \times 16 \times 3$ experiments. Therefore, we used a quantum linear layer consisting of 96 circuits for all one-to-one encodings cases, and 3 circuits for the amplitude encoding one.

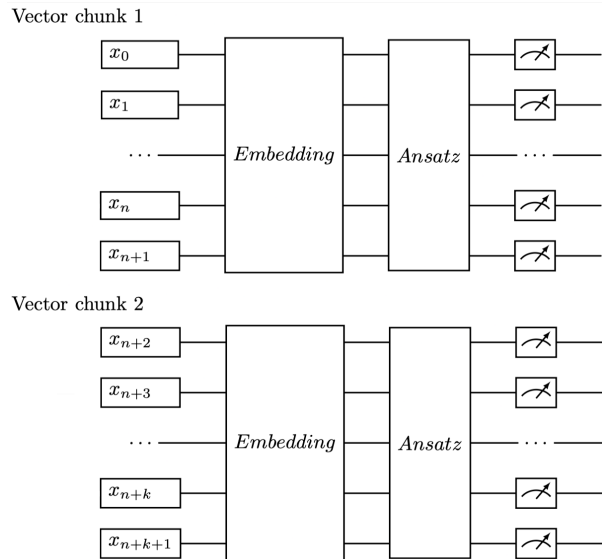


FIG. 3: Depiction of the quantum linear layer for processing vector \mathbf{x} with two circuits. The circuits independently process their corresponding vector chunk and can be run in parallel.

B. Hybrid models II: HQNN-Quantv

The *HQNN-Quantv* model follows the high-level blueprint of Senokosov *et al.* [6] but embeds it in the depth hierarchy of VGG16 [27], replacing the very first classical convolution with a bank of small, parameter-tied quantum circuits (see FIG. 4b). Every input image is split channel-wise into a dense grid of overlapping patches of size $qks \times qks$ (we study quantum-kernel size $(qks)=2, 3$ with stride 1). Each patch is flattened, normalised and loaded into a register of $Q = qks^2$ qubits with one of the encodings introduced in Sec. B. Because the same circuit parameters are reused for every spatial position and colour channel, the layer acts as a genuine quantum analogue of weight-tied convolution.

Inside each register we apply two identical blocks of a variational ansatz. These blocks are deep enough to mix local features but shallow enough to keep simulation tractable; their parameters, shared across all patches, are the only quantum learnable weights. Upon exit every qubit is measured once in the X , Y , or Z basis, yielding Q scalars per patch. Aggregating those scalars across the full grid produces $C \times Q$ feature maps of size $H' \times W'$, where H' and W' are the patch indices. Here C is the number of colour channels that are processed independently ($C = 3$ for RGB images). A fixed ReLU is applied and the tensor is passed to two classical 3×3 convolutions, global average pooling and a pair of fully connected layers that emit softmax probabilities for the EuroSAT classes.

The learnable weights split into two groups: a small set P_q of rotation angles inside one patch circuit, and the usual classical weights P_c that follow. Because the *same*

circuit is reused for every patch, P_q stays fixed when we move from 32×32 to 16×16 images or change the stride, while P_c matches the classical head already described for HQNN-Parallel. In practice P_q is only a few hundred parameters; roughly 10–100 times fewer than the weights in a classical first convolution that produces the same number of channel. Yet, it still injects a strong non-linearity at every pixel location.

C. Pure quantum models I: QCNN

QCNNs were first introduced in [9]. This model performs both the feature extraction and the classification with concatenated quantum operations, so the full model is represented as a unique quantum circuit (see FIG. 4c).

It draws inspiration from classical CNN and proposes doing convolutions via 2-qubit gates acting on adjacent qubits; followed by a pooling operation, which reduces the dimensionality by tracing out a subset of the qubits. It had great success due to its remarkable performance given its trainability [7, 29].

In this study, we did not want to consider an initial classical stage of dimensionality reduction, since the goal was to check how far we can go with only quantum components. Given limited computational resources, we did not want to exceed the range of 10 to 15 qubits; thus, we used amplitude embedding in order to be able to fit the images in the available number of qubits.

However, if we store the pixels in the amplitudes of the wavefunction, then the analogy of performing a convolution by 2-local gates needs to be looked at again. It turns out that if you track the way in which pixels are mixed in this scenario, you see that pixels from the same vicinity are indeed being mixed together (Appendix A), just like in a convolution. Moreover, by choosing the order in which the amplitudes are fed into the wavefunction, different kernel shapes can be implemented. In this work, we selected several orderings and checked their impact on the QCNN and a simplified model where the effect of the mixing is isolated: the Shaped Embedding Quantum Neural Network (SEQNN).

D. Pure quantum models II: SEQNN

To test the intuition that the order in which pixels are introduced into the amplitude of the state vector affects the way in which pixels are mixed, we built two simplified models.

FC

This model is used as a baseline, it consists of just a block with the structure described by the *Simplified Two Design* ansatz, which we used as a fully connected layer in the QCNN architecture.

Two kernels

Consists of three parts (check FIG. 4d):

1. Two arbitrary unitary operations acting as convolutional filters: one operating on the first two qubits and the second one on the following pair of qubits.
2. A pooling operation: one of the qubits on which the arbitrary unitary operations are acting is traced out, that is, two in total.
3. A fully connected layer on all remaining qubits.

E. Experiments

For each architecture, we systematically evaluate all possible combinations of encoding, ansatz, and measurement methods under identical learning rates, batch sizes, and dataset parameters. This approach aims to isolate and assess the impact of architectural design choices while maintaining consistent hyperparameters. Although further optimization could enhance results, the primary objective of this study is to analyze the effects of these design decisions rather than pursuing performance maximization. See more details in TABLE I for the different encodings, ansätze and measurements used for each model.

The dataset comprises of 500 samples with an 80/20 split, leading to 50 examples per class. The hybrid architectures use both 32×32 and 16×16 pixel resolutions. The QCNN model exclusively utilizes 16×16 images to streamline computational requirements while maintaining essential feature extraction capabilities.

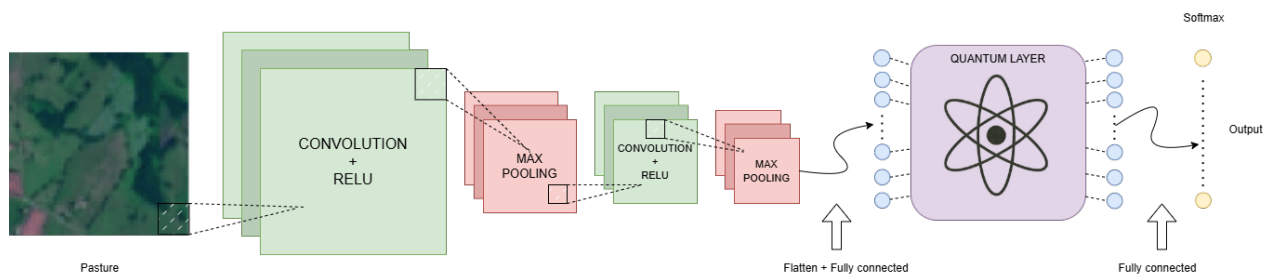
F. Metrics and optimization

We train our models using the schedule-free variant of the AdamW optimizer [30] coupled with the standard Cross Entropy Loss [31]. For evaluation, we report classification accuracy throughout the experiments. Additional metrics (e.g., precision, recall, F1-score) were computed using the scikit-learn library [32], and detailed definitions can be found in its documentation.

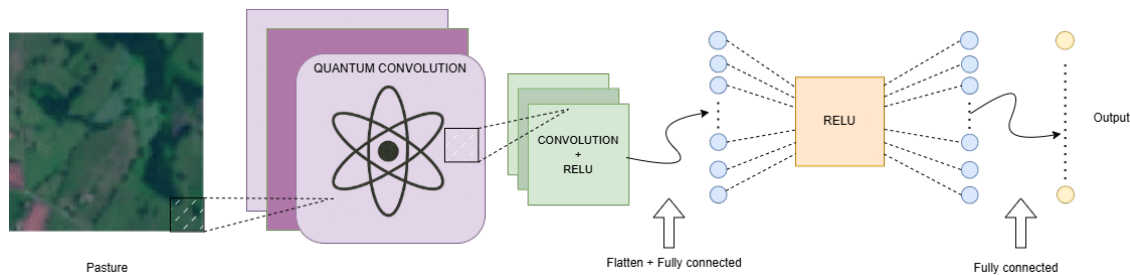
In all training runs we used the following hyperparameters: 0.01 learning rate, 16 batch size and 30 epochs with 10 epoch patience.

II. RESULTS

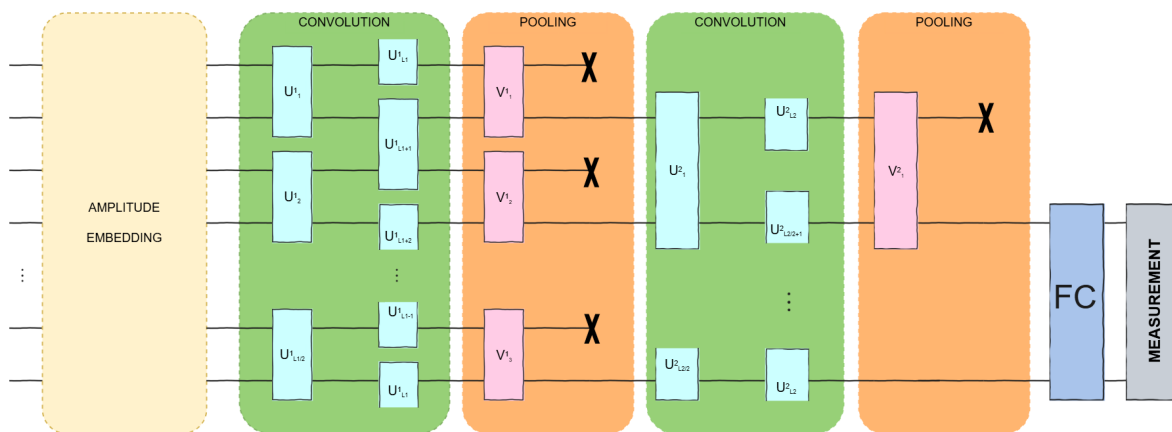
The data collected during these experiments provided critical insights into the system’s performance under varying conditions, thereby supporting the subsequent discussion of the results.



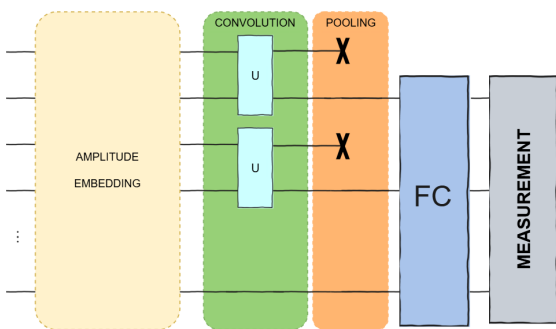
(a) HQNN-Parallel model from [6].



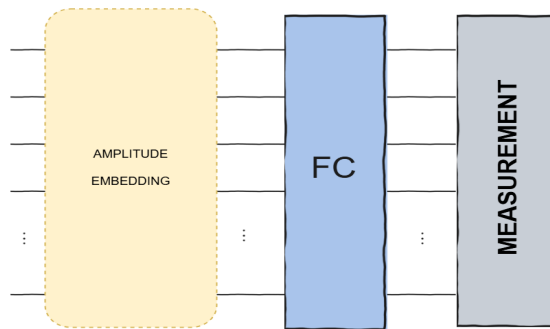
(b) HQNN-Quanv model inspired by [27].



(c) QCNN model from [9].



(d) Two kernels.



(e) FC model.

FIG. 4: Scheme of every model used. The three purely quantum models, c), d) and e), are particular cases of the generic PQC structure in Fig. 2. Quantum circuits were created using draw.io, an open-source library [28].

Model	Encodings	Variational ansätze	Measurements	Classical processing
<i>HQNN</i> <i>Parallel</i>	- Angle	- No entangled	- Pauli X	The model initially employs classical convolutional layers for feature extraction, followed by a quantum circuit integrated within the fully connected stage
	- Amplitude	- Fully entangled	- Pauli Y	
<i>HQNN</i> <i>Quantv</i>	- IQP	- Ring	- Pauli Z	After the <i>quantvolution</i> layer, the model proceeds with a classical convolutional layer to further extract features, followed by fully connected layers for classification
	- QAOA	- NQ		
	- Ring			
	- Waterfall			
<i>QCNN</i>	- Amplitude	- QCNN	- Pauli Z - Paulis - Histogram	None
<i>SEQNN</i>	- Amplitude	- Two kernel - FC (Simplified Two Design)	- Pauli Z - Paulis - Histogram	None

TABLE I: Summary of the models and their main components.

A. HQNN-Parallel

By selecting the best validation accuracy results for each encoding-ansätze combination, we observe that several hybrid configurations match or slightly exceed the classical baseline, as shown in FIG. 9. For instance, with 32×32 images, the IQP encoding combined with the no entangled variational circuit achieves 75.1% accuracy, outperforming the classical model's 67.1%.

In FIG. 10, we depict the learning behavior of the best-performing hybrid network and compare it with the classical model. The validation accuracy (FIG. 10c) shows that the best hybrid mode achieves better results than the classical one. However, the validation loss (FIG. 10d) indicates that both models begin to overfit after a few epochs, as the loss starts to increase. Prolonged training would likely exacerbate this issue.

We will now analyze how each component of the circuit influences the final performance.

How does the encoding influence?

Regarding the encoding method, no single solution is universally optimal. However, as seen in FIG. 5, the *RX*, *RY* and *QAOA Z* encodings exhibit lower variance in their performance. In contrast, the *Z* rotation-based encoding (*RZ*) consistently fails, yielding only 10% accuracy. As mentioned in the description of angle encoding, this is due to the encoding only adding an irrelevant global phase.

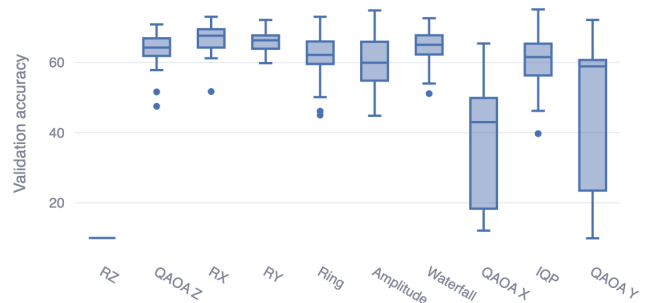


FIG. 5: Validation accuracy of all configurations for a fixed encoding.

How does the ansatz influence?

For the variational part of the circuit, we find that all tested ansätze yield similar performance, as illustrated in FIG. 11a. The median and maximum accuracies are comparable across all configurations. This suggests that for this particular problem, the choice of entangling structure within the ansatz is not a critical factor for achieving high accuracy.

How does the measurement influence?

The choice of measurement basis also shows a relatively small impact on the overall performance. As shown in FIG. 11b, all measurement strategies produce

similar accuracy distributions. There is a slight tendency for measurements in the computational basis to perform better than measurements in the X or Y bases, but the difference is not substantial.

B. HQNN-Quantv

By selecting the best validation accuracy results for each encoding-ansatz combination, we observe that none of the outcomes surpass the classical case. However, as illustrated in FIG. 13, certain combinations exhibit performance very close to the classical baseline. Although these results are derived in a simulated context, they provide insights into the types of circuits that should be considered in QML. We will analyze how each circuit type influences the outcomes.

In FIG. 14 depict the best network’s learning behavior and corresponding losses compared with the classic ones. As shown in the validation loss, there is a point at which both the classical and hybrid models cease to learn, leading to an increase in loss. Furthermore, our analysis indicates that the train performance continues to improve during training. However, allowing additional training epochs may lead to overfitting, as prolonged learning could cause the model to excessively adapt to the training data rather than generalizing effectively.

How does the encoding influence?

As we can see in FIG. 6, the amplitude and QAOA encodings fail to capture relevant features. In contrast, Waterfall, Ring and Angle encodings demonstrate greater utility for this task, although they yield slightly inferior performance compared to the classical approach. These findings suggest that, when quantum information is available, the aforementioned encodings should be prioritized for implementing *quantvolutions* of this type. The IQP encoding occupies an intermediate position, indicating potential scenarios where its application could be advantageous.

In this case we ignored the Z rotations of angle encoding because of the same explained before in section II.A.1

How does the ansätze influence?

Non entangled circuits are less effective than entangled ones. In the FIG. 15a, the bulk of accuracies for the no entangled ones obtains a worse performance than for the other 3 that do have at least some entanglement. Through this approach, we observe that image features are more effectively captured by leveraging the phenomenon of entanglement.

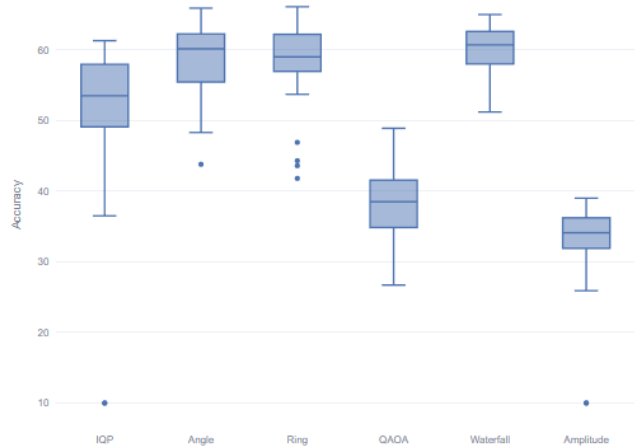


FIG. 6: Validation accuracy comparison across encodings. Image shapes (32×32 and 16×16) and quantum kernel shapes ($\text{qks} = 2, 3$) are included.

How does the measurement influence?

Preliminary results suggest that the type of measurement employed does not significantly affect the outcomes, as similar values are observed when evaluating the results. See FIG. 15b.

How does the quantum kernel shape influence?

Prior to conducting the experiments, we expected substantial differences in results depending on the qks , as the circuits employed qks^2 qubits. However, it was not the case, we see similar accuracies for $\text{qks} = 2, 3$, maybe a little better for shape 3 (FIG. 16a). The results for a qks of size 5 remain pending due to the high computational cost associated with a 25-qubit simulated circuit.

How does the image size influence?

Results suggest that image size does not significantly impact the model’s accuracy. This observation highlights a potential advantage, as reduced-resolution images appear to retain sufficient discriminative information comparable to higher-resolution counterparts. However, it is critical to acknowledge that these experiments utilized extremely small images, which may limit the broader applicability of this conclusion and warrant further investigation under diverse image-scale conditions. See FIG. 16b.

C. QCNN

How does the encoding influence?

Changing the ordering in the amplitude embedding to random tends to decrease the accuracy (See FIG. 17). This is less evident in the QCNN and FC architectures, as they were not designed to exploit this property. We are only showcasing here the best performing ordering against a random one, which we considered a baseline.

Although our *FC* model is supposed to mimic an unstructured fully connected layer, it is composed of adjacent two-qubit gates; hence, it is also affected by the change in ordering.

How does the measurement influence?

Within each group of measurements used for the quantum architectures, there is still room for some flexibility. In the *PauliZ* and *histogram* type of measurements, in some cases there are more active qubits than needed at the end; and in the *Paulis*, when measuring N qubits, we have in general $4^N - 1$ non-trivial pauli operators to select from. The choice of operator can greatly influence the classification accuracy as well; however, we are picking one at random in the study due to the vast range of possibilities.

In general, the best performing type of measurement was the *PauliZ*, which required measuring as many qubits as classes. Pauli's measurement gives the most flexibility at the cost of a great dispersion depending on the chosen operators (FIG. 19).

How does the FC layer deep influence?

We also tested whether increasing the number of parameters of the circuits by making the *FC* layers deeper influenced the performance of the models. Interestingly, we saw no improvement when increasing the number of parameters for 4 classes, suggesting that architectural changes are needed to enhance model classification capabilities (See FIG. 20). However, for 10 classes, increasing the depth of the *FC* layer did have a positive impact in the accuracy. A quick look at the training curves (FIG. 18) points towards the fact that we are indeed well in the underparameterization regime (all purely quantum models have less than 400 parameters).

III. EVALUATION

This section reflects on the qualitative lessons that emerged once the quantitative sweep of circuit configurations was complete, explaining *why* certain components matter and how they interact.

A. Hyperparameters

In this work, we did not consider adjusting the hyperparameters due to the associated computational cost. Future research should explore various combinations of these, such as the number samples used for training, optimizer, learning rate...

Additionally, it would be beneficial to investigate how these hyperparameters affect metrics beyond validation accuracy like generalization and potential barren plateaus. This analysis could provide deeper insights into optimizing our models and improving their performance in practical applications.

B. Could we use these models for other types of dataset?

In our study, we utilized the EuroSAT dataset of satellite images [5]. However, this dataset serves more as a means to an end rather than the primary focus of our work. It is suggested that these results may be extrapolated to other types of imagery, potentially yielding slightly better or worse outcomes but exhibiting similar behaviours.

C. Position of the quantum layer and effective entanglement

Hybrid models present two distinct forms of adding the quantum layers to classical networks.

When the layer is positioned in the latter part of the model, it operates on the features extracted by the earlier layers. With this approach, we found that the performance was slightly better than the classical counterpart, suggesting that increasing the qubits allocated per circuit, which would enable long-range correlations between features, could allow for better potential performance.

Conversely, situating the PQC-based convolutional layer at the beginning of the model led to a marginally worse performance than its classical counterpart. Suggesting that operating directly on raw pixels might not be optimal and alternative representations or preprocessing should be explored.

We found entanglement to be necessary for achieving top validation accuracy performance for the HQNN-Quantv architecture. In all cases where a non-entangling encoding and ansatz were used the performance was worse than the entangled alternatives. For the HQNN-Parallel, in some cases the non-entangled combination of ansatz and encoding was slightly better than some entangled versions. However, we would expect entangling combinations to perform better for higher qubit counts, as in our experiments each circuit only had access to 8/768 features.

These observations should be taken with a grain of salt, given that for the hybrid models we only measured

local observables and outcomes could be very different for other type of measurements.

D. Encoding, measurement and their interplay

For both hybrid models we found the encoding to be the most determining factor, FIG. 5, 6. Exceeding the effect of both ansatz and measurement, FIG. 11, 15.

We speculate this is due to several factors. First, the encoding is known to be a double edge sword: low complexity encodings don't have enough expressive power [33] while excessively complex encodings lead to data concentration [34], which limits the distinguishability of encoded states. Secondly, we tried few ansätze compared to encodings. Perhaps, by adding a range of carefully selected options with varying complexities the impact would be more clear. Lastly, local measurements on Pauli $X/Y/Z$ may be too simple to meaningfully affect performance.

Amplitude encoding thrived only when the circuit processed a compressed global representation; it faltered whenever it was fed directly with small pixel windows, because normalising entire patches dilutes the very gradients that early layers should preserve.

Single-qubit rotation encodings, by contrast, maintained robust performance regardless of placement, showing that locality in the data-to-state map is valuable whenever the network itself is still local.

For hybrids, the measurements were significantly less decisive, which is logical as they are highly similar to each other and can be interconverted via single-qubit rotations. Therefore three Cartesian single-qubit bases produced practically identical scores, implying that the subsequent classical layers rotate whatever Bloch-vector projection they are given. In a purely quantum network, where no further classical post-processing is available until the final softmax, the simplest global measurement in the computational basis offered the clearest separation of classes, whereas multiqubit Pauli strings introduced unnecessary complexity without a matching gain. The study was not particularly exhaustive in this aspect, and given that these measurements are more distinct from one another than in the previous case, it is reasonable to expect increased variability among them.

Interestingly, the fully quantum architectures used only amplitude encoding, yet a simple re-ordering of amplitudes before the first convolution layer delivered a noticeable lift. By arranging neighbouring pixels so that two-qubit gates act on semantically related amplitudes, the circuit effectively implements shaped kernels, mirroring how classical convolutions exploit spatial proximity.

E. Practical implications and open questions

When validation accuracy is plotted against the number of trainable parameters, the classical baselines re-

veal the familiar pattern of saturating returns. The fully quantum models, however, achieve the same operating point while maintaining an order-of-magnitude smaller parameter budget. Although present-day simulation makes wall-clock training slower, the marked reduction in learnable weights hints at a tangible memory advantage for future quantum accelerators. The promising aspect here is the remarkably small size of the model and the significant results it can achieve with so few parameters. The accuracy-parameter ratio is substantially higher compared to classical counterparts.

Several avenues remain open. First, the sweet-spot in entanglement may drift once realistic hardware noise is included, so repeating the sweep on early fault-tolerant devices would clarify the hardware-aware optimum. Moreover, analyzing the nonstabilizerness of the states generated by the different encodings and ansätze may shed light onto which combinations are best suited to provide value with respect to the classical counterpart. Efforts are already being made to study the behavior of such metrics in the context of PQCs [35]. Second, data re-uploading layers—whose parameters modulate the encoding itself—could compensate for the shortcomings of an early quantization by learning a task-specific Fourier spectrum. Finally, a systematic survey of measurement strategies under realistic noise models is still lacking; understanding which observables remain informative when decoherence is present will be key to deploying quantum classifiers in practice.

IV. CONCLUSION

The study addresses the challenge of understanding how design choices in PQCs, such as data encoding, variational ansätze, and measurement bases, affect the performance of quantum and hybrid neural network architectures in image classification tasks using the EuroSAT dataset [5].

Hybrid models are most sensitive to data encoding strategies, with amplitude-based embeddings being incompatible with certain architectures (e.g., HQNN-Quanv) but effective in others (e.g., HQNN-Parallel). Variational ansätze and measurement bases have a secondary impact but the entangled ansätze, better in HQNN-Quanv than HQNN-Parallel. Purely quantum models, constrained to amplitude encoding, show performance dependence on the combination of measurement strategies and input ordering. These last models are considerably smaller than the current classics.

Beyond merely enhancing current results, purely quantum models hold the promise of achieving exceptionally high accuracy-parameter ratios compared to existing methods. With adequate resources, this could lead to significantly lighter models with reduced computational overhead. Such advancements would enable more efficient and scalable QML applications, making them accessible for a broader range of practical use cases. This shift could revolutionize fields such as image

recognition, natural language processing, and complex data analysis.

We are limited to a specific dataset and predefined PQC configurations, which may not generalize to other tasks or quantum hardware. Additionally, the evaluation does not account for potential hardware-specific constraints or noise effects in quantum computations.

As future work, it would be interesting to consider the aforementioned points; like adjusting hyperparameters or even exploring different image datasets. On the other hand, a thorough analysis of the parameter-accuracy relationship will be crucial to select a suitable model for implementation in quantum computers.

This study not only identifies determinants in the performance of hybrid and quantum models, but also highlights how well-designed quantum circuits can overcome traditional barriers, bringing us closer to a future where QML is accessible and effective in complex industrial problems.

ACKNOWLEDGMENTS

The authors would like to express their gratitude for the collaborative efforts within the ARQA Cervera Technology Transfer Network [15]. This work is a result of the collective contributions and support from all members of this network, which has significantly enhanced our research outcomes.

OB is a fellow of Eurecat’s “Vicente López” PhD grant program.

We would like to thank Andrés García Mangas and Marco Aguado Acevedo for his support in launching and executing the experiments using the *CTIC Quantum Testbed (QUTE)* platform [11].

CODE AND DATA AVAILABILITY

All code and data used to generate the results presented in this paper are publicly available on GitHub at <https://github.com/uriballo/QML-Satellite-Image-Classification>.

-
- [1] M. Schuld, I. Sinayskiy, and F. Petruccione, *Contemporary Physics* **56**, 172 (2014).
 - [2] P. Wittek, *Quantum Machine Learning: What Quantum Computing Means to Data Mining* (Academic Press, 2014).
 - [3] J. Biamonte, P. Wittek, N. Pancotti, P. Rebentrost, N. Wiebe, and S. Lloyd, *Nature* **549**, 195 (2017).
 - [4] M. Schuld and F. Petruccione, *Supervised Learning with Quantum Computers*, Quantum Science and Technology (Springer Cham, 2018).
 - [5] P. Helber, B. Bischke, A. Dengel, and D. Borth, *IEEE Journal of Selected Topics in Applied Earth Observations and Remote Sensing* **12**, 2217 (2019).
 - [6] A. Senokosov, A. Sedykh, A. Sagingalieva, B. Kyriacou, and A. Melnikov, *Machine Learning: Science and Technology* **5**, 015040 (2024).
 - [7] T. Hur, L. Kim, and D. K. Park, *Quantum Machine Intelligence* **4**, 3 (2022).
 - [8] H. Elhag, K. Jansen, L. Nagano, and D. T. Alice, *arXiv* (2024), 10.48550/arxiv.2408.08701.
 - [9] I. Cong, S. Choi, and M. D. Lukin, *Nature Physics* **15**, 1273 (2019).
 - [10] J. Bowles, S. Ahmed, and M. Schuld, *arXiv* (2024), 10.48550/arxiv.2403.07059.
 - [11] A. García Mangas and R. Alonso, “Qute: Collaborative experimentation platform for quantum computing,” CTIC software v3.1 (2025).
 - [12] V. Bergholm, J. Izaac, M. Schuld, C. Gogolin, S. Ahmed, V. Ajith, M. S. Alam, G. Alonso-Linaje, B. AkashNarayanan, A. Asadi, J. M. Arrazola, U. Azad, S. Banning, C. Blank, T. R. Bromley, B. A. Cordier, J. Ceroni, A. Delgado, O. D. Matteo, A. Dusko, T. Garg, D. Guala, A. Hayes, R. Hill, A. Ijaz, T. Isacsson, D. Ittah, S. Jahangiri, P. Jain, E. Jiang, A. Khandelwal, K. Kottmann, R. A. Lang, C. Lee, T. Loke, A. Lowe, K. McKiernan, J. J. Meyer, J. A. Montañez-Barrera, R. Moyard, Z. Niu, L. J. O’Riordan, S. Oud, A. Panigrahi, C.-Y. Park, D. Polatajko, N. Quesada, C. Roberts, N. Sá, I. Schoch, B. Shi, S. Shu, S. Sim, A. Singh, I. Strandberg, J. Soni, A. Száva, S. Thabet, R. A. Vargas-Hernández, T. Vincent, N. Vitucci, M. Weber, D. Wierichs, R. Wiersema, M. Willmann, V. Wong, S. Zhang, and N. Killoran, “PennyLane: Automatic differentiation of hybrid quantum-classical computations,” (2022).
 - [13] A. P., S. Gross, F. Massa, A. Lerer, J. Bradbury, G. Chanan, T. Killeen, Z. Lin, N. Gimelshein, L. Antiga, A. Desmaison, A. Köpf, E. Yang, Z. DeVito, M. Raison, A. Tejani, S. Chilamkurthy, B. Steiner, L. Fang, J. Bai, and S. Chintala, “Pytorch: An imperative style, high-performance deep learning library,” (2019), *arXiv:1912.01703 [cs.LG]*.
 - [14] European Space Agency, “Copernicus: Europe’s eyes on earth,” (n.d.).
 - [15] Red ARQA, “Red de excelencia cervera arqa: Computación cuántica aplicada a la innovación empresarial,” (2024).
 - [16] M. Schuld, I. Sinayskiy, and F. Petruccione, *Quantum Information Processing* **13**, 2567 (2014).
 - [17] Y. Cao, G. G. Guerreschi, and A. Aspuru-Guzik, *arXiv* (2017), 10.48550/arXiv.1711.11240.
 - [18] E. Knill, *arXiv preprint* (1995), 10.48550/arXiv.quant-ph/9508006.
 - [19] V. Havlíček, A. D. Córcoles, K. Temme, A. W. Harrow, A. Kandala, J. M. Chow, and J. M. Gambetta, *Nature* **567**, 209 (2019).
 - [20] S. Lloyd, M. Schuld, A. Ijaz, J. Izaac, and N. Killoran, “Quantum embeddings for machine learning,” (2020).
 - [21] F. A. Venturelli, *Quantum neural networks for data-efficient image classification*, Laurea magistrale, Università di Bologna (2023), corso di Studio in Physics [LM-DM270].

- [22] M. Schuld, A. Bocharov, K. M. Svore, and N. Wiebe, *Physical Review A* **101** (2020), 10.1103/PhysRevA.101.032308.
- [23] T. Hur, I. F. Araujo, and D. K. Park, *Physical Review A* **110** (2024), 10.1103/PhysRevA.110.022411.
- [24] M. Cerezo, A. Sone, T. Volkoff, L. Cincio, and P. J. Coles, *Nature Communications* **12**, 1791 (2021).
- [25] J.-G. Liu and L. Wang, *Physical Review A* **98**, 062324 (2018).
- [26] S. Y.-C. Chen, H.-H. Tseng, H.-Y. Lin, and S. Yoo, “Learning to program quantum measurements for machine learning,” (2025).
- [27] K. Simonyan and A. Zisserman, arXiv preprint (2014), 10.48550/arXiv.1409.1556.
- [28] J. Wilkens, “Quantum circuit draw.io library,” (2021).
- [29] A. Simen, C. Flores-Garrigos, N. N. Hegade, I. Montalban, Y. Vives-Gilabert, E. Michon, Q. Zhang, E. Solano, and J. D. Martín-Guerrero, *Physical Review Research* **6**, L042060 (2024).
- [30] A. Defazio, X. A. Yang, H. Mehta, K. Mishchenko, A. Khaled, and A. Cutkosky, “The Road Less Scheduled,” (2024).
- [31] PyTorch, *CrossEntropyLoss — PyTorch 2.5 documentation* (2024).
- [32] F. Pedregosa, G. Varoquaux, A. Gramfort, V. Michel, B. Thirion, O. Grisel, M. Blondel, P. Prettenhofer, R. Weiss, V. Dubourg, J. Vanderplas, A. Passos, D. Cournapeau, M. Brucher, M. Perrot, and E. Duchesnay, *Journal of Machine Learning Research* (2011).
- [33] M. Schuld, R. Sweke, and J. J. Meyer, *Physical Review A* **103**, 032430 (2021), 2008.08605.
- [34] G. Li, R. Ye, X. Zhao, and X. Wang, arXiv preprint arXiv:2303.11332 (2023), 10.48550/arXiv.2303.11332.
- [35] C. Capecci, G. C. Santra, A. Bottarelli, E. Tirrito, and P. Hauke, arXiv preprint arXiv:2505.17185 (2025).

Appendix A: Shaped Embedding Quantum Neural Network, detailed explanation

In this section we will show how we can use the action of a two-qubit gate acting on adjacent qubits to implement convolutional kernels over the original images by selecting the way in which pixels are introduced in the amplitudes of the state vector.

1. The math behind

The action of a general two qubit gate is given by

$$\mathcal{G}|\varphi\rangle = \begin{pmatrix} g_{00} & g_{01} & g_{02} & g_{03} \\ g_{10} & g_{11} & g_{12} & g_{13} \\ g_{20} & g_{21} & g_{22} & g_{23} \\ g_{30} & g_{31} & g_{32} & g_{33} \end{pmatrix} \begin{pmatrix} \varphi_0 \\ \varphi_1 \\ \varphi_2 \\ \varphi_3 \end{pmatrix} = \begin{pmatrix} \vec{g}_0 \cdot \vec{\varphi} \\ \vec{g}_1 \cdot \vec{\varphi} \\ \vec{g}_2 \cdot \vec{\varphi} \\ \vec{g}_3 \cdot \vec{\varphi} \end{pmatrix} \quad (\text{A1})$$

where $\vec{\varphi} = (\varphi_0, \varphi_1, \varphi_2, \varphi_3)$ and \vec{g}_i corresponds to the i -th row of \mathcal{G} . Thus, each row of the matrix representing the gate can be seen as a kernel acting on the four entries of the two-qubit state vector. Now, if we have three qubits and perform a gate on the two right-most ones,

$$\mathbb{I}_0 \otimes \mathcal{G}_{1,2}|\varphi\rangle = \begin{pmatrix} \mathcal{G} & \mathbf{0}_{2 \times 2} \\ \mathbf{0}_{2 \times 2} & \mathcal{G} \end{pmatrix} |\varphi\rangle = \begin{pmatrix} \begin{pmatrix} \vec{g}_0 \\ \vec{g}_1 \\ \vec{g}_2 \\ \vec{g}_3 \end{pmatrix} \cdot \vec{\varphi}_0 & \mathbf{0}_{2 \times 2} \\ \mathbf{0}_{2 \times 2} & \begin{pmatrix} \vec{g}_0 \\ \vec{g}_1 \\ \vec{g}_2 \\ \vec{g}_3 \end{pmatrix} \cdot \vec{\varphi}_1 \end{pmatrix} \quad (\text{A2})$$

where $\vec{\varphi}_0 = (\varphi_0, \varphi_1, \varphi_2, \varphi_3)$, $\vec{\varphi}_1 = (\varphi_4, \varphi_5, \varphi_6, \varphi_7)$. The full 8-element state vector is arranged in groups of four pixels which are mixed together by the corresponding kernels associated with the rows of the gate.

If the gate acts on the left-most qubits, we are still implementing kernels that mix amplitudes of the state vector, but now these groups are not comprised of subsequent amplitudes. More explicitly:

$$\mathcal{G}_{0,1} \otimes \mathbb{I}_2 = \begin{pmatrix} g_{00} \begin{pmatrix} 1 & 0 \\ 0 & 1 \end{pmatrix} & g_{01} \begin{pmatrix} 1 & 0 \\ 0 & 1 \end{pmatrix} & g_{02} \begin{pmatrix} 1 & 0 \\ 0 & 1 \end{pmatrix} & g_{03} \begin{pmatrix} 1 & 0 \\ 0 & 1 \end{pmatrix} \\ g_{10} \begin{pmatrix} 1 & 0 \\ 0 & 1 \end{pmatrix} & g_{11} \begin{pmatrix} 1 & 0 \\ 0 & 1 \end{pmatrix} & g_{12} \begin{pmatrix} 1 & 0 \\ 0 & 1 \end{pmatrix} & g_{13} \begin{pmatrix} 1 & 0 \\ 0 & 1 \end{pmatrix} \\ g_{20} \begin{pmatrix} 1 & 0 \\ 0 & 1 \end{pmatrix} & g_{21} \begin{pmatrix} 1 & 0 \\ 0 & 1 \end{pmatrix} & g_{22} \begin{pmatrix} 1 & 0 \\ 0 & 1 \end{pmatrix} & g_{23} \begin{pmatrix} 1 & 0 \\ 0 & 1 \end{pmatrix} \\ g_{30} \begin{pmatrix} 1 & 0 \\ 0 & 1 \end{pmatrix} & g_{31} \begin{pmatrix} 1 & 0 \\ 0 & 1 \end{pmatrix} & g_{32} \begin{pmatrix} 1 & 0 \\ 0 & 1 \end{pmatrix} & g_{33} \begin{pmatrix} 1 & 0 \\ 0 & 1 \end{pmatrix} \end{pmatrix} = \begin{pmatrix} g_{00} & 0 & g_{01} & 0 & g_{02} & 0 & g_{03} & 0 \\ 0 & g_{00} & 0 & g_{01} & 0 & g_{02} & 0 & g_{03} \\ g_{10} & 0 & g_{11} & 0 & g_{12} & 0 & g_{13} & 0 \\ 0 & g_{10} & 0 & g_{11} & 0 & g_{12} & 0 & g_{13} \\ g_{20} & 0 & g_{21} & 0 & g_{22} & 0 & g_{23} & 0 \\ 0 & g_{20} & 0 & g_{21} & 0 & g_{22} & 0 & g_{23} \\ g_{30} & 0 & g_{31} & 0 & g_{32} & 0 & g_{33} & 0 \\ 0 & g_{30} & 0 & g_{31} & 0 & g_{32} & 0 & g_{33} \end{pmatrix} \quad (\text{A3})$$

$$\mathcal{G}_{0,1} \otimes \mathbb{I}_2|\varphi\rangle = \mathcal{G}_{0,1} \otimes \mathbb{I}_2 \begin{pmatrix} \varphi_0 \\ \varphi_1 \\ \varphi_2 \\ \varphi_3 \\ \varphi_4 \\ \varphi_5 \\ \varphi_6 \\ \varphi_7 \end{pmatrix} = \begin{pmatrix} \vec{g}_0 \cdot \vec{\varphi}_0 \\ \vec{g}_0 \cdot \vec{\varphi}_1 \\ \vec{g}_1 \cdot \vec{\varphi}_0 \\ \vec{g}_1 \cdot \vec{\varphi}_1 \\ \vec{g}_2 \cdot \vec{\varphi}_0 \\ \vec{g}_2 \cdot \vec{\varphi}_1 \\ \vec{g}_3 \cdot \vec{\varphi}_0 \\ \vec{g}_3 \cdot \vec{\varphi}_1 \end{pmatrix} \quad (\text{A4})$$

and $\vec{\varphi}_0 = (\varphi_0, \varphi_2, \varphi_4, \varphi_6)$, $\vec{\varphi}_1 = (\varphi_1, \varphi_3, \varphi_5, \varphi_7)$.

Conclusion: for $N + 1$ qubits, there are 2^{N+1} amplitudes, and 2^{N-1} groups of 4 amplitudes that are being mixed together by the action of a gate operating on two adjacent qubits. If the two-qubit gate is in position p , the 2^{N-1} groups of 4 amplitudes are:

$$\vec{\varphi}_l^{(p)} = (\varphi_l, \varphi_{l+2^p}, \varphi_{l+2 \cdot 2^p}, \varphi_{l+3 \cdot 2^p}), \quad l \in \{0, \dots, 2^{N-1}\}. \quad (\text{A5})$$

It is worth noting that with the same kind of reasoning we can see that a general unitary acting of three adjacent qubits can implement a kernel that mixes $2^3 = 8$ amplitudes of the state vector and, in general, we can create a kernel over 2^K pixels with a gate operating on K adjacent qubits.

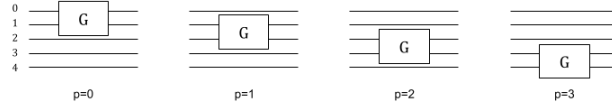
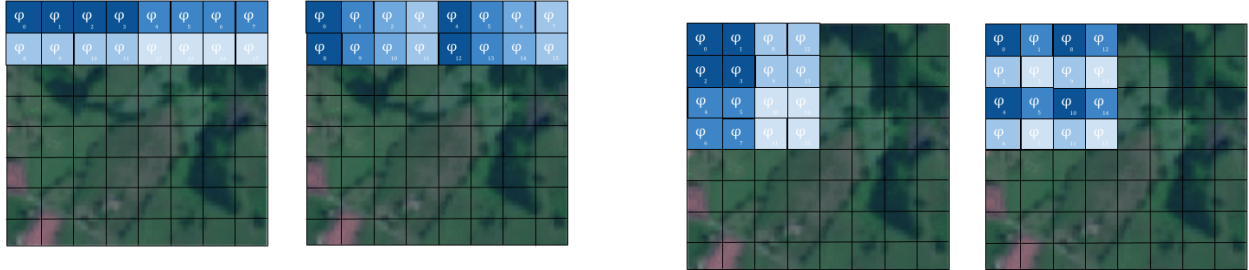


FIG. 7: The four possible positionings of a two-qubit gate acting on adjacent qubits of a 5-qubit register.

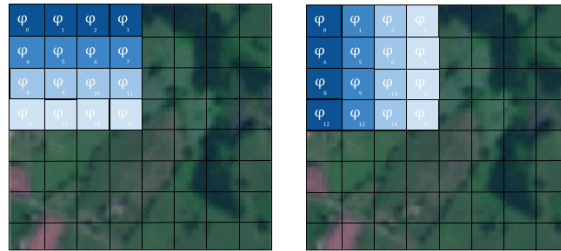
2. Custom orderings

As a first attempt to try to test the idea explained in the last section, we designed specific orderings for the initial amplitude embedding such that it would leverage the action of adjacent two qubit gates to implement some kernels.



(a) Flattening the image array in a row first fashion corresponds with a kernel that acts on horizontal lines (first gate) and mixes every fourth pixel (second gate).

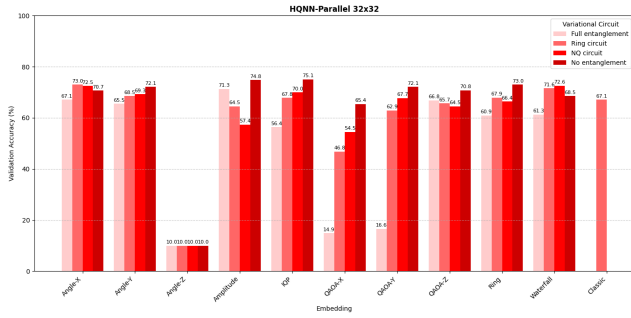
(b) This ordering implements a kernel that acts on squared regions of the images.



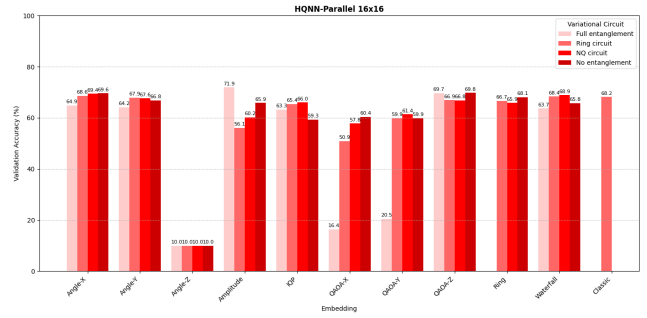
(c) With this particular ordering we can mix both vertical and horizontal lines over the image.

FIG. 8: Diagram of how the pixels are ordered in the amplitudes of the state vector of the N -qubit circuit. For each ordering, the picture on the left (right) represents the which pixels the first (second) gate is mixing. Pixels shaded with the same color are mixed together.

Appendix B: HQNN Parallel Hybrid model

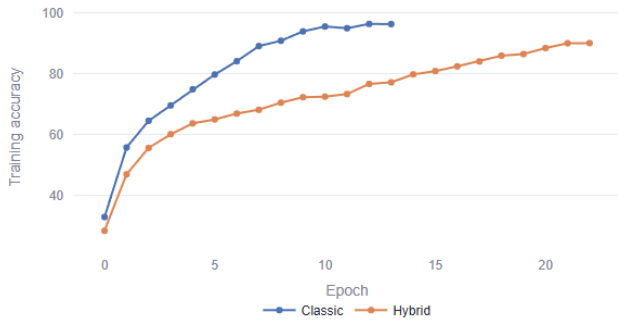


(a) Best validation accuracies for 32 × 32 images.

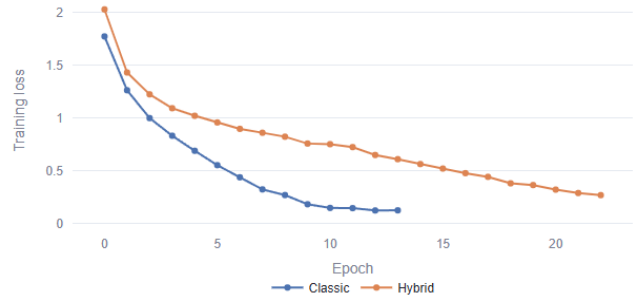


(b) Best validation accuracies for 16 × 16 images.

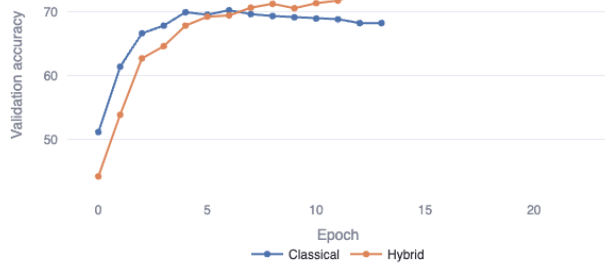
FIG. 9: Best validation accuracies with the HQNN-Parallel model. The result has been taken for the best combination encoding-ansätze and for the best measurement.



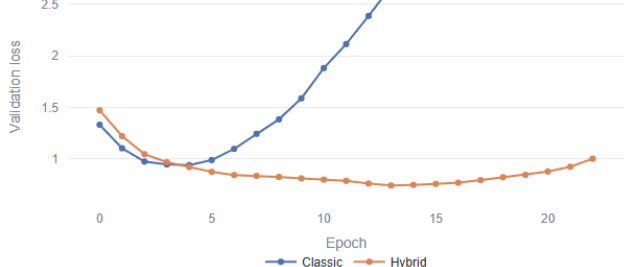
(a) Train Accuracy.



(b) Train Loss.

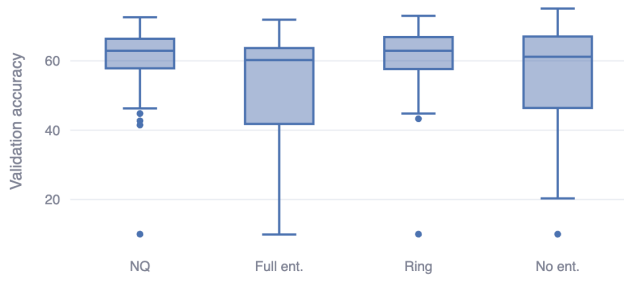


(c) Validation Accuracy.

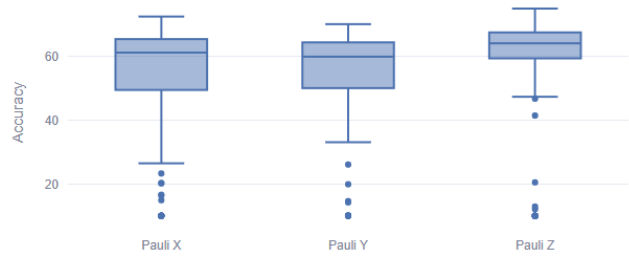


(d) Validation Loss.

FIG. 10: Training and validation accuracy and loss for the best hybrid model compared with the classic one.



(a) Validation accuracy of all configurations for a fixed ansätze.



(b) Validation accuracy of all configurations for a fixed measurement.

FIG. 11: Validation accuracies for different measurements and ansätze.

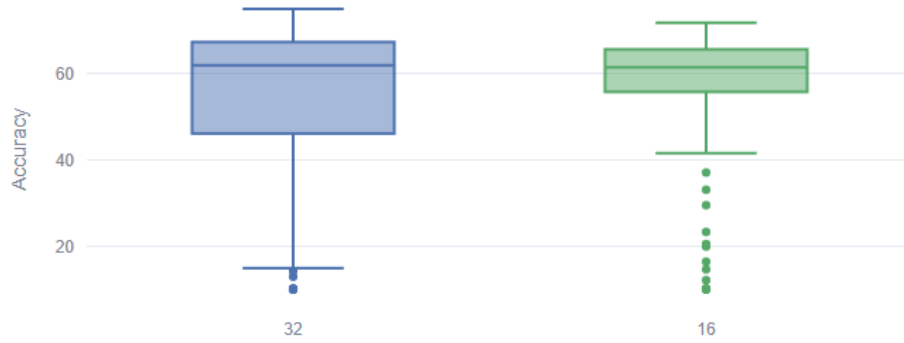
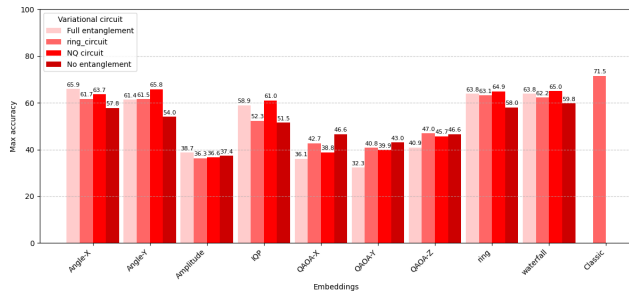
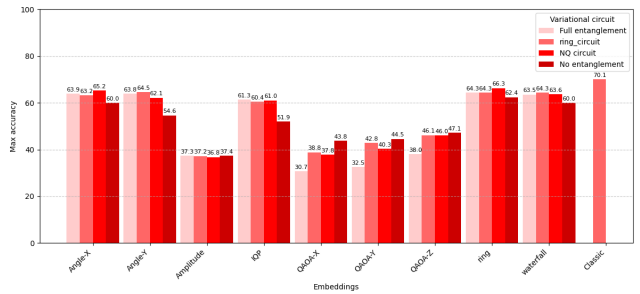


FIG. 12: Validation accuracy across 32×32 and 16×16 image size.

Appendix C: HQNN-Quany model results

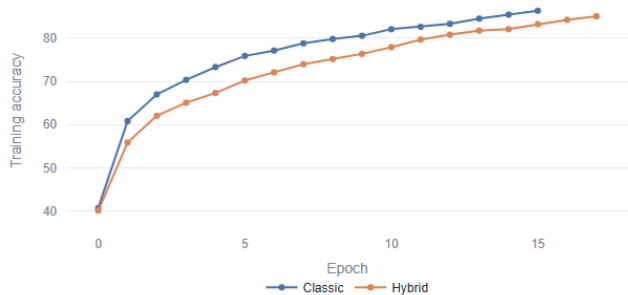


(a) Best validation accuracies for 32×32 images and $qks = 3$.

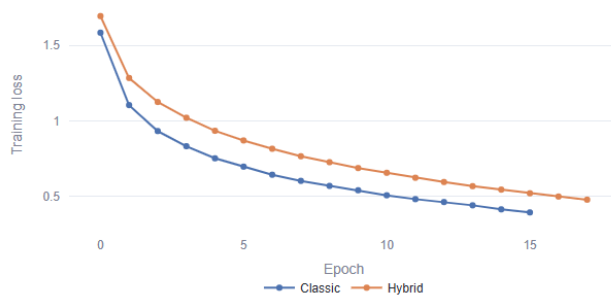


(b) Best validation accuracies for 16×16 images and $qks = 3$.

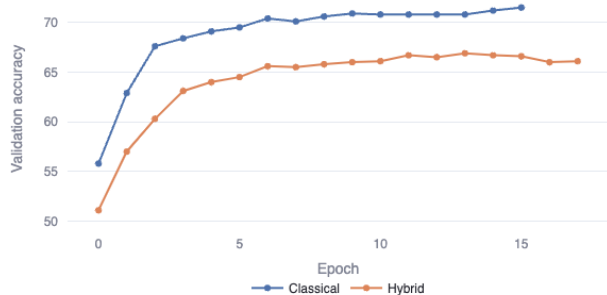
FIG. 13: Best validation accuracies with the HQNN-Quany model. The result has been taken for the best combination encoding-ansätze and for the best measurement.



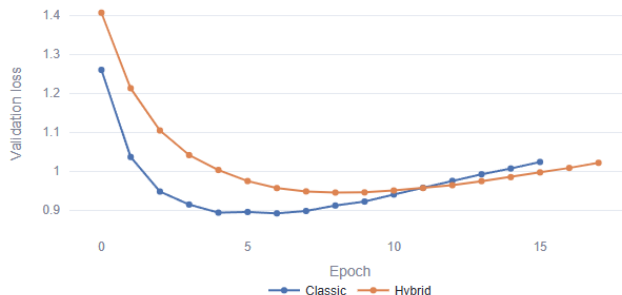
(a) Train Accuracy.



(b) Train Loss.

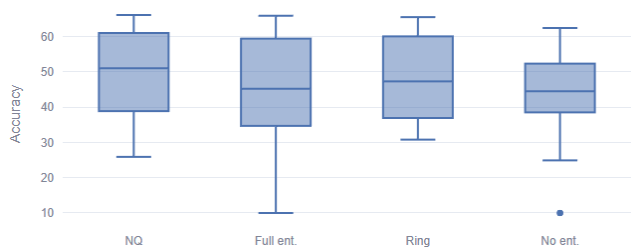


(c) Validation Accuracy.

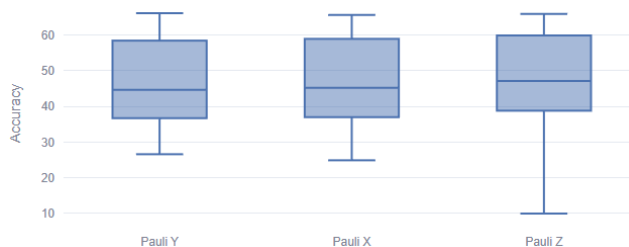


(d) Validation Loss.

FIG. 14: Train and validation accuracy and loss for the best hybrid model compared with the classic one.

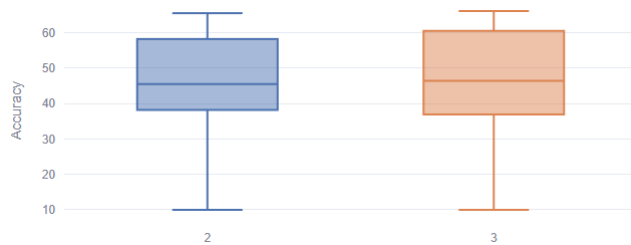


(a) Ansätze.



(b) Measurements.

FIG. 15: Validation accuracy comparison across ansätze and measurements. Image shapes (32×32 and 16×16) and quantum kernel shapes ($qks = 2, 3$) are included.



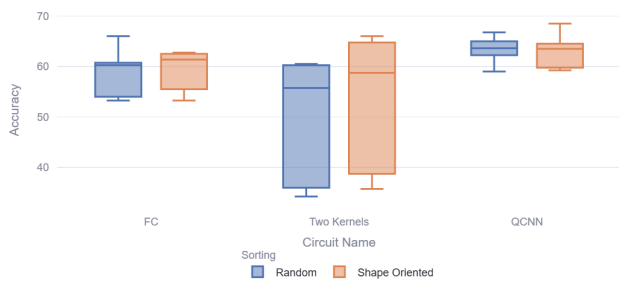
(a) QKS shapes.



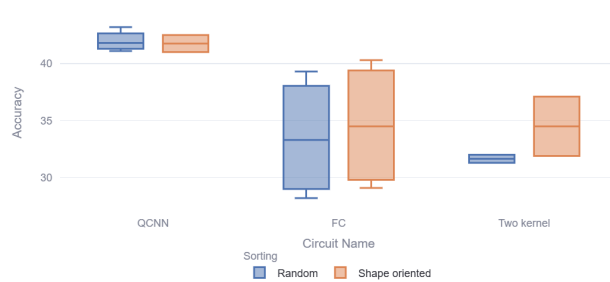
(b) Image size: 32×32 and 16×16 .

FIG. 16: Validation accuracy comparison across different QKS shapes and image size.

Appendix D: Pure quantum models results

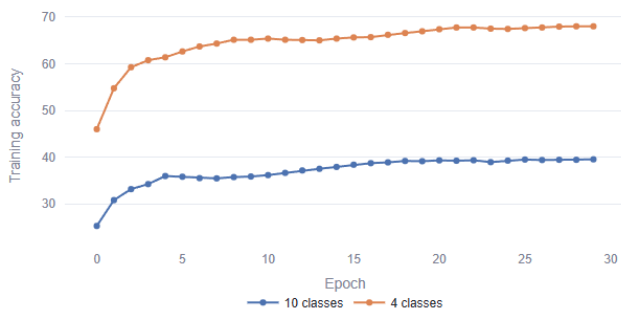


(a) Orderings, 4 classes.

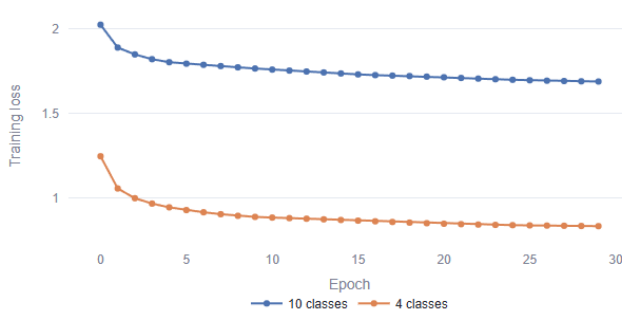


(b) Orderings, 10 classes.

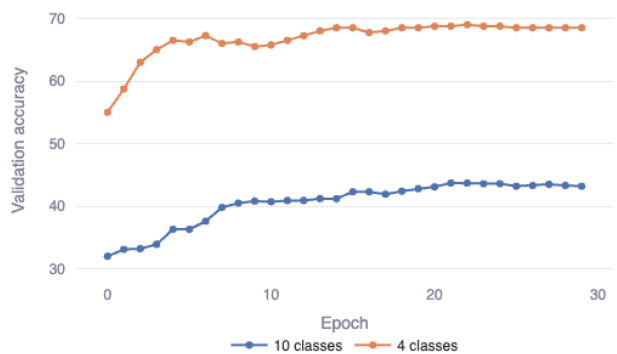
FIG. 17: Validation accuracy comparison across different orderings for 4 and 10 classes separately.



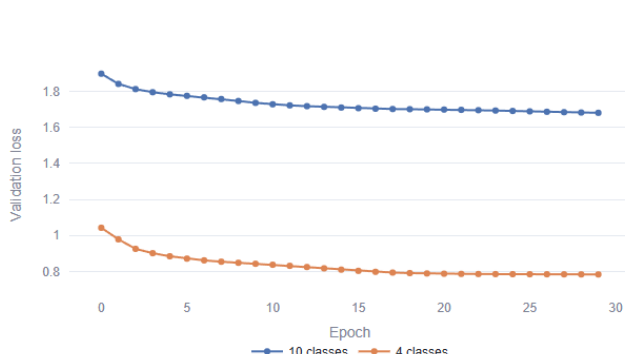
(a) Train Accuracy.



(b) Train Loss.



(c) Validation Accuracy.



(d) Validation Loss.

FIG. 18: Training and validation accuracy and loss for the best purely quantum model for 4 and 10 classes.

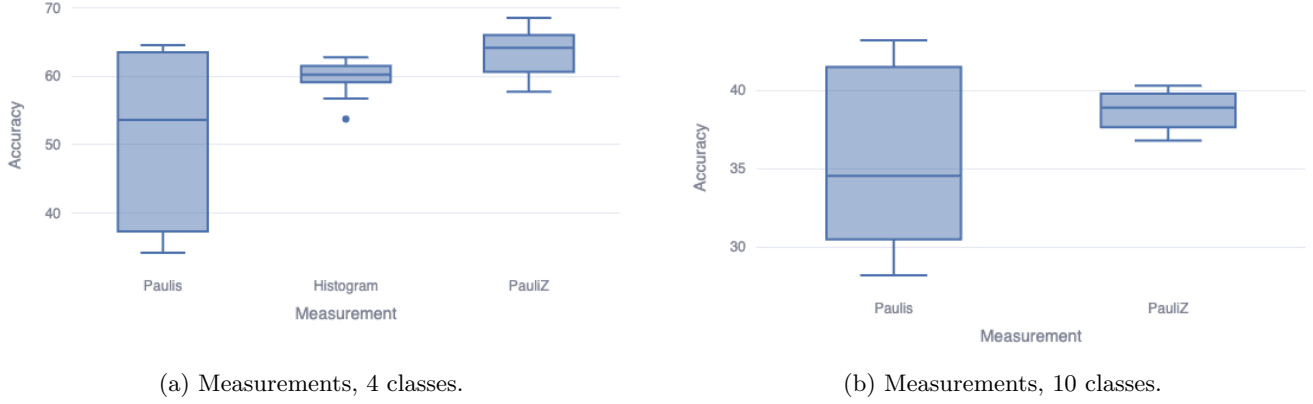
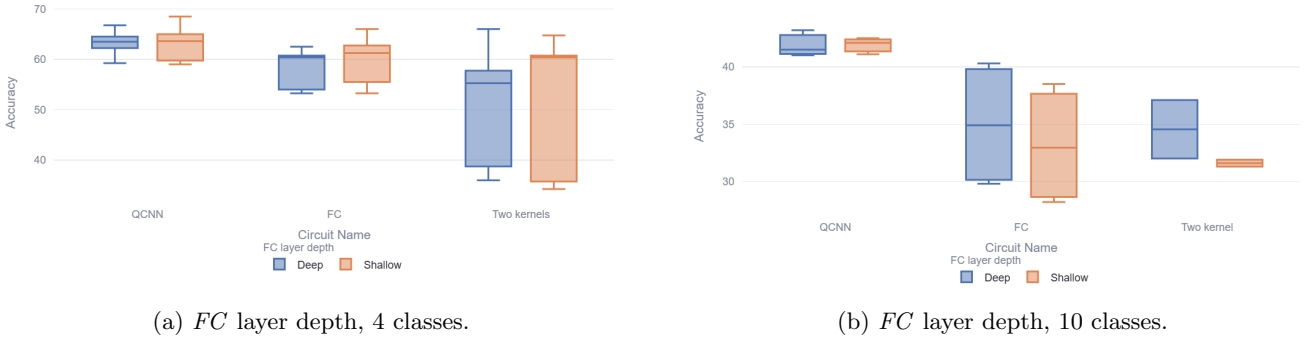


FIG. 19: Validation accuracy comparison across measurements for 4 and 10 classes separately.

FIG. 20: Validation accuracy comparison across *FC* layer depth for 4 and 10 classes separately.

Appendix E: QCNN and SEQNN, full results overview

Ansatz	Ordering	Measurement	4 classes	10 classes	N params
QCNN	Random	histogram	59	-	300
		PauliZ	65	-	293
		Paulis	63,75	42,1	300
	Flatten	histogram	59,75	-	300
		PauliZ	68,5	-	293
		Paulis	63,5	42,5	300
Two kernel	Random	histogram	60,5	-	184
		PauliZ	60,25	-	184
		Paulis	34,25	31,3	184
	Squared	histogram	60,75	-	184
		PauliZ	64,75	-	184
		Paulis	35,75	31,9	184
FC (Simplified Two Design)	Random	histogram	60,25	-	190
		PauliZ	66	36,8	190
		Paulis	53,25	28,2	190
	Squared	histogram	62,75	-	190
		PauliZ	62,25	38,5	190
		Paulis	55,5	29,1	190

TABLE II: Validation accuracy results for shallow FC layer.

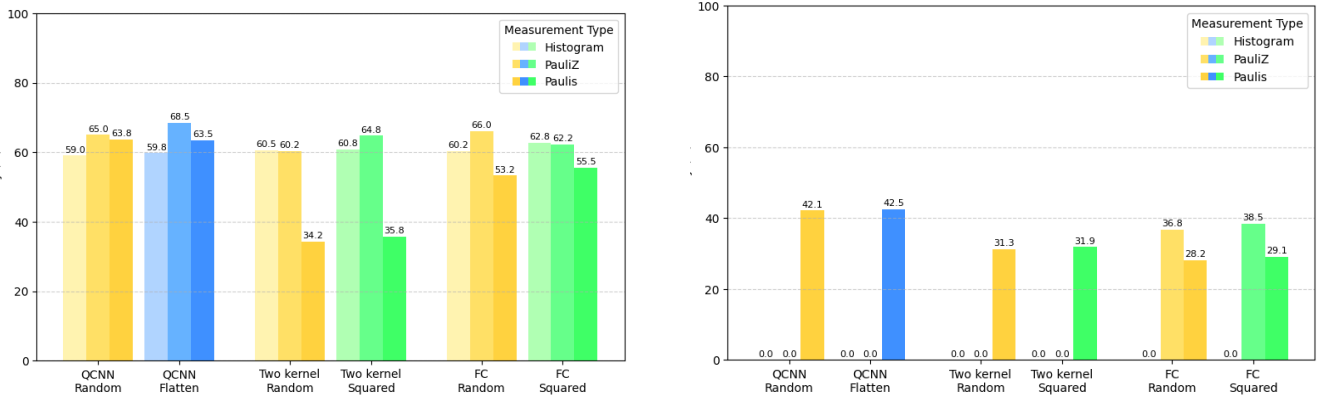


FIG. 21: Validation accuracy by Ansatz, Ordering, and Measurement type for 4 and 10 classes respectively. Shallow FC layer.

Ansatz	Ordering	Measurement	4 classes	10 classes	N params
QCNN	Random	histogram	62,25	-	326
		PauliZ	66,75	-	373
		Paulis	63,5	41,5	316
	Flatten	histogram	59,25	-	326
		PauliZ	63,5	-	373
		Paulis	64,5	41	316
Two kernel	Random	histogram	53,75	-	-
		PauliZ	57,75	-	310
		Paulis	36	32	-
	Squared	histogram	56,75	-	-
		PauliZ	66	-	310
		Paulis	38,75	37,1	-
FC (Simplified Two Design)	Random	histogram	60,25	-	-
		PauliZ	60,75	39,3	352
		Paulis	54	29,8	-
	Squared	histogram	62,5	-	-
		PauliZ	60,5	40,3	352
		Paulis	53,25	30,5	-

TABLE III: Results for deep FC layer.

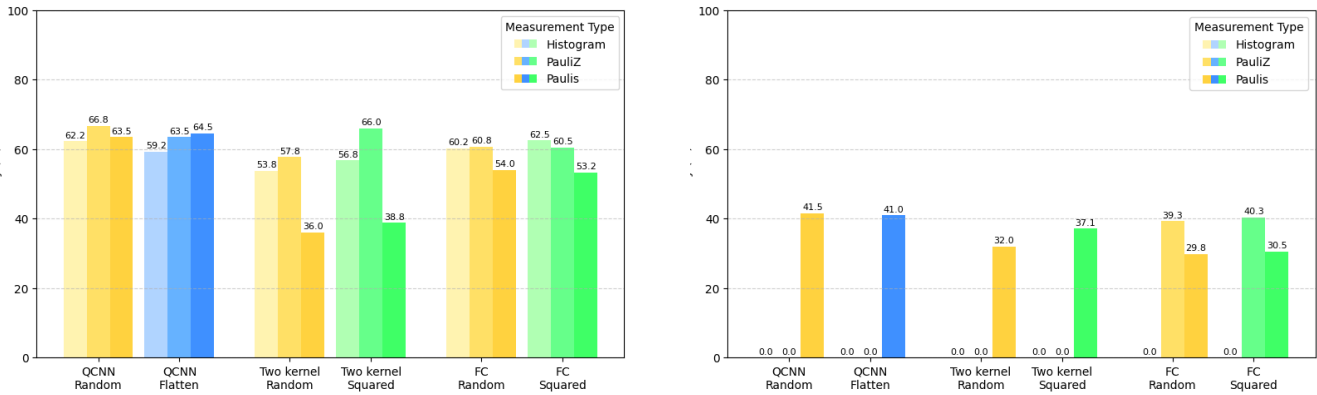


FIG. 22: Validation accuracy by Ansatz, Ordering, and Measurement type for 4 and 10 classes respectively. Deep FC layer.